Deeply buried ancient volcanoes control hydrocarbon migration in the South China Sea

Qiliang Sun[1,2,3*], Christopher A.L. Jackson[4], Craig Magee[5], and Xinong Xie[1,3]

[1]Key Laboratory of Tectonics and Petroleum Resources, China University of Geosciences (Wuhan), Ministry of Education, Wuhan 430074, China;

[2]Laboratory for Marine Mineral Resources, Qingdao National Laboratory for Marine Science and Technology, Qingdao 266061, China;

[3]College of Marine Science and Technology, China University of Geosciences (Wuhan), Wuhan, Hubei 430074, PR China;

[4]Basins Research Group (BRG), Department of Earth Science & Engineering, Imperial College, London, SW7 2BP, UK;

[5]School of Earth and Environment, University of Leeds, Leeds, LS2 9JT, UK

Abstract

Buried volcanoes are increasingly identified in the sedimentary basins both on lands and continental margins. However, their roles on the post-eruption fluid flows are still poorly understood, which greatly influence the estimate of seal integrity and increase the hydrocarbon exploration/production risks. Here we use high-resolution 3D seismic reflection and borehole data from the northern South China Sea to show that ancient (Miocene) volcanoes, buried several

*Corresponding author: Dr. Qiliang Sun
Telephone/fax: +86 27 67886167
E-mail address: sunqiliang@cug.edu.cn.

kilometers below the seabed and fed by magma exploiting underlying, rift-related faults, controlled the bulk permeability of hydrocarbon seal rocks. Differential compaction and doming of strata above these large (up to 10 km diameter by 590 m tall), igneous rock-cored volcanoes promoted the formation of post-eruption extensional faults. Seismic reflection and borehole data suggest hydrocarbons produced by more deeply buried source rocks were either trapped within the volcanoes and/or in porous strata overlying them, with the supra-volcano faults acting as long-lived hydrocarbon migration pathways. Considering that volcanism and related deformation are both common on many magma-rich passive margins, the interplay between the magmatic products and hydrocarbon migration documented here may be more common than currently thought. More specifically, volcanoes may locally degrade seal quality and facilitate cross-stratal migration of hydrocarbons from source to reservoir.

Keywords

Hydrocarbon leakage, volcano, volcanism, faulting, seal integrity, South China Sea

Introduction

Extrusive and intrusive igneous rocks are widespread in sedimentary basins formed by lithospheric stretching (e.g. Berndt et al., 2000; White et al., 2003; Jackson et al., 2013; Magee et al., 2016). Magma-related fluids, such as those released from hydrocarbon-rich source rocks in response to intrusion-induced heating or derived directly from the magma itself, can migrate to shallower levels within the basin, and may even be expelled into the ocean or atmosphere (e.g. Hasenclever et al., 2017; Moussallam et al., 2017). For example, the synchronous, widespread injection of methane-rich hydrothermal fluids, emanating from the tips of intruding igneous sills, and extrusion from vents formed at the palaeosurface have been suggested to drive climate change (e.g. Svensen et al., 2004, 2012; Iyer et al., 2017). Fractured intrusive bodies can form fluid migration pathways long after their emplacement and solidification (Rateau et al., 2013; Schofield et al., 2017), potentially diverting fluid into and reactivating extrusive vent and volcanic systems (Holford et al. 2017). Understanding our igneous systems focus later (i.e. post-magmatic) fluid is critical to de-risking hydrocarbon exploration targets in magma-rich, petroliferous basins.

Deciphering how igneous systems influence later fluid flow events is problematic, because the physical properties (e.g. porosity and permeability) of intrusive and extrusive rocks can be highly heterogeneous over a range of scales (Millett et al., 2016), and related bodies can either act as reservoirs (e.g. Yang et al., 2016) or seals (e.g. Holford et al., 2012). Moreover, differential compaction of sedimentary rocks across (nearly) incompressible igneous rocks characterizing can cause folding and faulting (e.g. Zhao et al., 2014; Holford et al., 2017), which can facilitate long-lived, post-magmatic fluid flow (Holford et al., 2017). A particular problem, which we try to address here, is that there are very few studies describing the precise control volcanoes and related overburden deformation has on post-magmatic fluid flow. Knowledge derived from such examples would greatly reduce the risk associated with hydrocarbon exploration.

Here we use high-resolution 3D seismic data and borehole data to analyze the spatial and temporal relationships between buried, Early Miocene volcanoes, pre- and post-eruption normal faults, and post-eruption free gas accumulations in the northern South China Sea (SCS). Our study highlights that the buried volcanoes not only drove post-eruption overburden deformation, but also controlled gas migration pathways long after the volcanoes became dormant.

Geological setting

The SCS is the largest (>3,500,000 km^2) and deepest (>5,000 m of water depth) marginal sea in the western Pacific Ocean. Seafloor spreading initiated in the northeast SCS in the Early Oligocene (~ 32.0 Ma) in response to the Nanhai Event (e.g. Franke, 2013), before propagating to the southwest and ceasing at 15.0-15.5 Ma (Briais et al., 1993; Li et al., 2014). Post-spreading magmatism in the SCS has obscured seafloor spreading fabrics, making it difficult to precisely identify the timing of cessation of seafloor spreading (Sibuet et al., 2016).

The Pearl River Mouth Basin is one of several Cenozoic rift basins located on the northern continental margin of the SCS, covering an area of ~17.5×10^4 km^2, and comprising several NE-trending grabens, half grabens, and flanking massifs (Fig. 1a). During continental rifting (Late Cretaceous - Early Oligocene), non-marine mudstones and coals, which now represent the main hydrocarbon source rocks within the region, were deposited in the fault-bound depocentres sags (Zhang & Huang, 1991; Huang et al., 2003). During the syn-to-post rift transition (Late Oligocene - Early Miocene), marginal marine sandstones were deposited; these form the most important hydrocarbon reservoir units and carrier beds in the Pearl River Mouth Basin (Zhu et al., 2009). During this phase, the Nanhai Event caused three active periods of normal faulting (32-29 Ma, 23.8-21.0 Ma, and 18.5-16.5 Ma), which can be tied to initial opening, ridge jump, and maximum extension events in the SCS ocean basin (Deng et al., 2018). Deposition during the subsequent period of post-rift thermal subsidence (Early Miocene - Present), was dominated by very fine-grained, pelagic and hemipelagic strata, which provide an excellent regional seal (Zhu et al., 2009). The latest Dongsha Event, triggered by the collision of the Philippine Sea Plate with the

Eurasian Plate, occurred from 10.5 Ma onwards, generating extensional faulting in relatively young strata (Lüdmann & Wong, 1999; Zhao et al., 2012).

The SCS lacks seaward-dipping reflectors (SDRs) and can thus be classified as magma-poor rifted margin (Yan et al., 2006; Franke, 2013). However, post-rift magmatism, in the form of sills and relatively small, mafic-intermediate volcano complexes, are documented (e.g. Zou et al., 1995; Yan et al., 2006; Franke, 2013; Li et al., 2014; Lester et al., 2014; Sun et al., 2014b; Zhao et al., 2014, 2016, 2018; Ma et al., 2018; Deng et al., 2018). Given their spatial and temporal relationship, Early Miocene volcanoes and normal faults may have been genetically related (Deng et al., 2018).

Data and Methods

We use a high-resolution 3D seismic dataset covering an area of ~530 km^2, in water depths of ~500-1200 m. It was acquired in 2010 by a 3000 m long streamer with 240 channels. The dataset has a bin spacing of 12.5 m for both N-S oriented inlines and E-W oriented crosslines. The data is zero-phase processed and displayed with SEG (Society of Exploration Geophysicists) normal polarity, whereby a downward increase in acoustic impedance corresponds to a positive reflection (red on displayed seismic profiles). We use borehole data (well loggings, core cuttings, micropaleontologies) from BY7-1 to determine the lithology and age of the volcano-bearing succession and, thus, the age of volcano emplacement (Fig. 2). These borehole data also constrained interval velocities for the volcanic complexes (~4500 m/s) and surrounding strata (~2800 m/s). The dominant frequency within the seismic data gradually decreases downwards from the seabed to ~35 Hz where the volcano complexes are located. Based on these frequency and velocity data, we estimate an approximate vertical resolution of ~32 m and ~20 m for the volcanic complexes and surrounding sedimentary strata, respectively (Zhao et al., 2016). Accordingly, we estimate the detection threshold of the seismic data to be ~16 m for volcanic rock-bearing unit and ~10 m for sedimentary strata. For the shallow strata (<500 m), an estimated velocity of 1700 m/s and a dominant frequency of ~45 Hz suggest vertical resolution of ~10 m and detection limit of ~5 m.

We identify 14 mounded structures in the 3D seismic survey (Figs. 3, 4, 5a-b). One of these mounds was drilled in 1988 by exploration borehole BY7-1 (Figs. 2, 5a) (Qin, 2000). This well shows that the mounded structure is mainly composed of basalt and tuff, interbedded with a thin limestone layer and a thin claystone layer (Qin, 2000; Zhao et al., 2016; Ma et al., 2018) (Fig. 2); we therefore interpret the mounded structure is of volcanic origin. The volcano is ~17.1±2.5 Ma based on K-Ar dating of a sample taken close to its top (Qin, 2000) (Fig. 2). Dead oil that is residual oil without its volatile components is identified from samples within the volcano, as well as within the interbedded limestone (Fig. 2). Sub-volcanic strata are mainly composed of sandstone interbedded with several layers of volcanic material (basalt/tuff) and claystone, with the lowermost (oldest) volcanic material attributed a K-Ar date of 35.5±2.78 Ma (Qin, 2000) (Fig. 2). A stratum above the volcano comprises a ~260 m thick, Early Miocene sandstone package overlain by Middle Miocene (and younger) claystones interbedded with several thin layers of sandstone and siltstone (Fig. 2).

Six regional stratigraphic boundaries were mapped and correlated to borehole BY7-1 (T0-T2 and T4-T6; e.g. Pang et al., 2007; Zhao et al., 2016; Deng et al., 2018; Ma et al., 2018) (Figs. 1b-c). We also define and map the top (TV) and base (BV) of the volcanic complexes; the former coincides with T5 (Figs. 2-4). To identify and map free gas and normal faults, we extracted RMS attribute and variance slices from the 3D seismic volume (Fig. 5). The former measures the reflectivity of a given thickness (window) of seismic data and it is calculated through the divide of square root of the sum of squared amplitudes with the number of samples within the specified window used (Brown, 2004) (Figs. 5f-j). The variance, which is operated within a time window/interval and converts a volume of continuity (the normal reflections) into a volume of discontinuity, is free of interpretive bias (Brown, 2004) (Figs. 5c-e).

Results

Volcanoes

The tops of the volcanoes are characterized by undulating, positive, high-amplitude seismic reflections (T5) (Fig. 4). The dips of the volcano flanks range from ~1º to ~14º, and are usually >10º. Some volcanoes have relatively flat tops (<1º) (Fig. 4a). Compared to their tops, the bases of the volcanoes are relatively flat (Figs. 4a-b, 4d) and are characterized by a continuous, high-amplitude seismic event (Fig. 4). The cores of the volcanoes are usually characterized by chaotic seismic reflections, and layered seismic reflections, the latter sometimes downlapping onto the basal surface (T5; Fig. 4). Similar facies and geometries are reported from volcanoes imaged in seismic data from offshore southern Australia (e.g. Jackson, 2012; Magee et al., 2013a; Reynolds et al., 2018) and the western Indian rifted margin (Calvès et al., 2011).

Individual volcanoes are circular or elliptical, with their long axis trending WNW (~301º) (Figs. 3, 5a-b). More importantly, several volcanoes are connected to form linear complexes that also trend WNW (~301º) (Figs. 3, 5a-b). The diameters of volcanoes range from ~1.0 km to ~6.0 km and their heights are between ~50 m and ~590 m (Figs. 5a-b). The volcanoes cover an area of at least ~245 km^2 and individually have a volume of at least ~62.5 km^3 (Fig. 5b).

The volcanoes are onlapped and draped by post-eruption sedimentary strata of the Early Miocene Zhujiang Formation (Figs. 1b, 4). Strata overlying the volcanoes are typically folded, with folds being ~1-3 km wide and having amplitudes of ~350-1100 m high. In some cases, seismic imaging is poor directly above the volcanoes due to velocity wipe-out zones that may be associated with anomalously low seismic frequencies (Figs. 4a, 6). The succession directly underneath the volcanoes are characterized by weak and chaotic seismic reflections (Figs. 4a-b), that are typically cut by normal faults (Figs. 1c, 7).

Normal faults

Normal faults are widely developed across the study area. We distinguish two fault populations based on their distribution relative to the volcanoes: those faults that predominantly occur beneath the volcanoes and those restricted to strata above the volcanoes.

Faults beneath volcanoes

Normal faults within sub-volcanic strata (i.e. below surface T5) typically strike WNW-ESE (300±15º) (Figs. Figs. 6b, 7c-d, 5e, 8a), similar to the overlying volcanoes (Figs. 3, 5b, 8b-c). Faults are, on average, ~1.4 km long, but may reach lengths of up to ~7.2 km (Figs. 8d, 8g). The faults are ~0.35-3.5 km tall (~85% are <1.1 km) and have throws of <160 m (Fig. 7c-d). Importantly, some of the largest normal faults (i.e. >3.0 km tall) in the pre-volcanic strata terminate directly beneath volcanoes (Figs. 6b, 7c-d) or suspected volcanoes ((Figs. 1c, 7c-d)), extending downwards into crystalline basement.

A few WNW-striking normal faults penetrate upwards from the basement to strata shallower than T0 (~2.58 Ma), crossing-cutting the level at which the volcanic complexes are developed (Fig. 4c). The vertical extent of these faults is >4.0 km (Fig. 4c), yet they are still relatively short (<6.1 km long) (Figs. 8e-f). These tall faults usually offset the volcanoes and are associated with supra-volcano growth strata (Figs. 4c, 7a-b).

Supra-volcanic faults

Most supra-volcanic normal faults (especially between T4 - T1) have limited vertical extents, ranging from ~0.3 km to 2.0 km tall (most, ~68%, are <1.2 km tall) (Figs. 4a, 4c-d). The average lengths of faults on seismic time slices at 1150 ms (Fig. 8e) and 1800 ms (Fig. 8f) are ~1.7 km and ~1.2 km, respectively. Moreover, most faults (~88%) are <3.0 km long, with the longest being ~6.1 km (Figs. 8e-f, h-i). The maximum displacement observed on the supra-volcanic faults is typically <90 m, with this value decreasing upwards towards the faults upper tip (Fig. 6). However, in some cases the fault displacement cannot be quantified, especially in cases where faults are poorly imaged below free gas (see section below). The most important observations for the post-eruption faults are that they best-developed and more closely spaced directly above the volcanic complexes (Figs. 4, 5c-d), some terminating immediately above the underlying volcanoes (Fig. 4a). Moreover, the gross strike of these faults (WNW-ESE; ~300±15º) (Figs. 8b-c) is similar to the trends of the underlying volcanic complexes (Fig. 3).

Free gas

Seismic reflection anomalies, characterized by anomalously low frequencies and negative polarity, are frequently observed in the seismic profiles (Fig. 4). These anomalies are either isolated at one particular stratigraphic level, or form vertical stacks spread across multiple stratigraphic levels. Nearly all seismic anomalies occur along the normal faults that cross-cut strata above volcanoes (Figs. 4, 5f, 5g-j). Based on their seismic characteristics (e.g. enhanced, low-frequency and negative-polarity seismic reflections), we interpret these seismic anomalies as representing areas of free gas (cf. Judd & Hovland, 2007; Cartwright et al., 2007). The seismic reflections directly above the volcanoes are quite weak and/or characterized by low frequencies (Fig. 4). So-called velocity 'push-downs' are frequently observed beneath the stacked free gas layers (Figs. 4a, 4c), which is indicative of low-acoustic velocities caused by free gas in the pore spaces (e.g. Judd & Hovland, 2007; Sun et al., 2012).

Free gas mainly accumulated within siltstone and sandstone strata penetrated by borehole BY7-1 (Fig. 2). These gas-charged layers are usually characterized by anomalously high sonic differential time values, consistent with seismic evidence (i.e. push-downs) for slower velocities (DT) (Fig. 2). Moreover, total gas is usually in excess of 30,000 ppm in gas-charged layers, which is higher than in those strata lacking gas. $\delta^{13}C$ values gradually decrease upward from the top of the drilled volcano (-34‰ PDB) (Fig. 2). However, it is >-55‰ (PDB) even in the shallowest strata, which indicates that the gas mainly thermogenic (e.g. Tissot & Welte, 1984; Zhu et al., 2009).

Discussions

Interaction between volcano complexes and normal faults

The volcano intersected by borehole BY7-1 formed in response to at least three eruptive episodes, separated by periods of deposition of interbedded limestone and claystone layers (Fig. 2). The occurrence of shallow-water limestone (Qin, 1996) between the eruptive products suggests volcanism occurred in shallow water, an interpretation consistent which previous observations (Zhao et al., 2016; Ma et al., 2018). Volcanism ceased ~16.5 Ma, given it is onlapped by surface T5 (~16.5 Ma) (Fig. 4) and that the analysis of samples recovered from its top is dated at 17.1±2.5 Ma (Qin, 2000) (Fig. 2).

The faults located within the sub-volcanic strata (i.e. below surface T5) are corresponding to those (~32-16.5 Ma) documented by Deng et al. (2018) in the adjacent Baiyun Sag (Fig. 1a). Therefore, most of them were active before or during the volcano eruption. The observations that volcanoes are spatially and directionally correlated with pre-eruption faults (Figs. 3, 5a-b, 5d, 6, 8a) and, commonly, in direct contact with underlying faults (Figs. 7c-d), suggest the faults may have facilitated magma ascent (e.g. Le Corvec et al., 2013; Magee et al., 2013b, 2016; Isola et al., 2014). Volcano growth fed by fault is further supported by the across-fault thickening of volcanic strata (red dashed ellipses in Figs. 7a-b). However, we cannot discount dykes as a potential mechanism for magma ascent, given such structures are not typically imaged in seismic reflection data (e.g. Phillips et al., 2017), and, if present, would be located within the very poorly imaged zone directly below the volcanoes (Figs. 4a-b, 6).

Supra-volcano faults (between surfaces T4 and T1; i.e. Middle-Late Miocene) are younger than the volcanoes (early Middle Miocene; ~16.5 Ma), with some structures being active in the Quaternary (i.e. they offset T0, which is ~2.58 Ma) (Fig. 4). The observations the supra-volcano faults are clustered above the volcanoes (Figs. 4, 5b-d), terminate down-dip at the tops of volcanoes (e.g. Fig. 4a) and have similar strikes to the volcano long-axes (Figs. 5b-d, 8b-c), suggest that the volcanoes influenced the location of later faulting. We consider two potential mechanisms may have driven supra-volcano faulting. First, the igneous rock-cored, and thus only weakly compactable rigid volcanoes, may have locally modified the regional stress field. The northern SCS experienced compression from the Philippine Plate in the east since the Middle Miocene (surface T3; ~13.8 Ma) (Sun et al., 2014a). This stress field likely triggered the WNW-oriented faulting (Figs. 8b-c) (Lüdmann & Wong, 1999; Sun et al., 2014a), with the volcanoes causing faults to preferential develop above them (Figs. 4, 6). A second mechanism again relates to the fact that the volcanoes are cored by weakly compactable, igneous rocks (Figs. 4, 6). However, in this model, differential compaction of weak sediments /sedimentary rock would have given rise to the formation of broad, low-amplitude folds situated directly above the buried volcanoes (Figs. 4a-b, 6). This folding could have triggered outer-arc extension-related normal faulting in strata above the long axis of the buried volcanoes as we observed in this study (Figs. 4a-b, 6). Note that the two models presented here are not mutually exclusive; both regional, extension-related stress and more local, differential compaction-related stress could have driven faulting above the buried volcanoes. For example, whilst the faults extend above observed regions of differential compaction folding, folding may have promoted fault nucleation with continued slip being driven by regional extension.

Focused fluid flow promoted by buried volcanoes and neotectonics

Our observations from seismic data (Figs. 4, 5f-5j), combined with borehole and geochemical data (Fig. 2), show that free gas is locally preserved in clastic layers located above the volcanoes (Fig. 9). The free gas is sharply bound by the normal faults, which is clearly observed in both RMS maps (Figs. 5f, 5g-j) and seismic profiles (Figs. 4, 6). These observations suggest the free gas likely migrated upward along these faults and charged the more porous layers (Fig. 9d). Considering the Baiyun Sag, which to located to the east of the study area (Fig. 1), is a hydrocarbon-rich 'kitchen' area with a sedimentary thickness of >10 km (e.g. Pang et al., 2008), thermogenic free gas is potentially sourced from there (Fig. 9d). It may have migrated from the deep-seated source rock in the Baiyun Sag to structural highs in the Yunkai Low Massif (study area) through permeable strata and/or unconformities along the western flank of the Baiyun Sag (Fig. 1a, Fig. 9d). The transported free gas possibly temporarily accumulated within the volcanoes, judged from the dead oil within the volcanoes (Fig. 2), or accumulated within the porous layers/structural traps above the volcanoes (Fig. 2). The latter is confirmed by the residual gas that is expressed as low p-wave velocities and high total gas readings (> 40,000 ppm) (Fig. 2). Post-eruption faulting reduced the bulk permeability of the potential seal, permitting hydrocarbon migration along faults to shallower structural levels (Fig. 4). It is however difficult to precisely constrain when hydrocarbon leakage from the volcanoes occurred. Considering the Dongsha Event started from ~10.5 Ma, peaking at ~5.3 Ma (Lüdmann & Wong, 1999; Zhao et al., 2012), gas leakage was also likely punctuated. The latest period of gas migration along the faults probably occurred in the Quaternary, based on the observations that the shallowest free gas occurs within uppermost Pliocene strata (Fig. 4b) and that many faults penetrate upward into Quaternary strata (Fig. 4).

Model for volcano-tectono interactions and related fluid flow

Here we propose a four-stage model to account for the link between magmatism, faulting and fluid flow in the northern SCS. In the first stage, magma is extruded onto land or the seabed in relatively shallow water (Qin, 1996; Yan et al., 2006) having ascended by deep-seated faults in the crystalline basement (Figs. 7c-d, 9a). Though one sample from the erupted materials was dated to 35.5±2.78 Ma (Qin, 2000), how long magmatism lasted cannot be determined, because the base of the volcanic pile is not penetrated, such that its age remains unknown.

During the second stage, coarse-grained terrigenous material was deposited, with intermittent periods of relatively weak volcanism (Figs. 2, 9b). Normal faulting (pre-eruption faulting) occurred in these terrigenous strata during this stage (Deng et al., 2018) and some of them probably penetrated into or were linked with the faults within the basement (Figs. 7, 9b). After this relatively quiescent second stage, a second main period of intense volcanic activity occurred, emplacing several volcanic complexes onto the shallow paleo-seabed (Fig. 9c); volcanoes emplaced in this third stage were probably also fed by magma ascending via the deep-seated faults (Fig. 7). Volcanism ceased in the study area before ~16.5 Ma.

During the fourth and final stage (~16.5 Ma onwards), thick sequences of predominantly very fine-grained clastic material were deposited above the volcanoes (Fig. 9d). Another main period of normal faulting occurred during this stage, and formed the supra-volcanic normal faults (Fig. 9d). Hydrocarbons sourced from the Baiyun Sag were transported along the flanks of Baiyun Sag through porous layers or along unconformities (Fig. 9d) (e.g. Pang et al., 2008; Zhu et al., 2009).

These hydrocarbons probably temporarily accumulated within the topographic highs generated by the volcanoes, before migrating upwards via the normal faults (Figs. 4, 6-7, 9d).

Implications

Drilling data indicates the volcanoes lack live oil (Fig. 2). However, the presence of dead oil and minor staining indicates that hydrocarbons likely migrated into and through the volcanoes. Whether the volcanoes served as reservoirs or simply as pathways for hydrocarbons, they clearly focused post-eruption fluid flow (Fig. 4). Folded strata above the mounds lay in four-way dip closures that likely acted as structural trap for fluids migrated upwards from the mounds or from the porous sediments/unconformity on their flanks (Fig. 9d). Along with the increase of overpressure within the trap, fluids would leak upwards through faults as documented in this study (Figs. 4, 9d). Buried volcano-related, focused fluid flow conduits could thus be more common than presently thought, since differential compaction-related domes and related structures (e.g. normal faults) are common above many ancient, seismically imaged volcanoes (e.g. Li et al., 2015; Yang et al., 2016; Schofield et al., 2017). The presence, evolution and importance of these coupled systems will likely become clearer as more 2D and 3D seismic reflection data become available within volcanically influenced basins. The risk of seal degradation, and secondary migration and accumulation of hydrocarbons related to buried volcanoes should be taken into consideration during hydrocarbon exploration in such basins.

Conclusions

We used high-resolution 3D seismic data and borehole data from the northern South China Sea to document the impact of faults on magma ascent and the spatial location of volcanic centers, and the role the latter have on fluid flow. Volcanism was multi-staged, ceasing before ~16.5 Ma (T5), with migration of hydrocarbons lasting until the Early Pleistocene (~2.58 Ma). Hydrocarbons migrated upwards along post-eruption faults, which are related to regional stress and the bending of strata caused by differential compaction. The transported fluids (mainly methane) finally charged porous layers (siltstone/sandstone) offset by the post-eruption faults. This study shows that the volcano-related deformations can influence the surrounding, regional stress fields and subsurface fluid flow. These processes likely increase the bulk permeability of otherwise sealing sequences, facilitating the cross-stratal migration of hydrocarbons from deep sources to shallower reservoirs. This study highlights the underappreciated role buried volcanoes may have on focused, subsurface fluid flow. Considering that buried volcanoes are widespread in both the passive and active continental margin basins, more attention should be placed on their role in controlling fluid flow.

Acknowledgements

This work was supported by the National Key R&D Program of China (No. 2018YFC0310000) the National Scientific Foundation of China (Grant Nos. 91528301, 41676051 and 41372112), and the Fundamental Research Funds for the Central Universities-the China University of Geosciences (Wuhan) (No. CUG160604). We thank the China National Offshore Oil Company for permission to release the data.

References

Aarnes, I., Podladchikov, Y., & Svensen, H. (2012). Devolatilization-induced pressure build-up: implications for reaction front movement and breccia pipe formation. *Geofluids*, 12, 265-279. doi: 10.1111/j.1468-8123.2012.00368.x.

Berndt, C., Skogly, O.P., Planke, S., Eldholm, O., & Mjelde, R. (2000). High-velocity breakup-related sills in the Vøring Basin, off Norway. *Journal of Geophysical Research-Solid Earth*, 105, (B12). doi: 10.1029/2000JB900217.

Briais, A., Patriat, P., & Tapponnier, P. (1993). Updated interpretation of magnetic anomalies and seafloor spreading stages in the South China Sea: implications for the Tertiary tectonics of Southeast Asia. *Journal of Geophysical Research-Solid Earth*, 98, 6299-6328. doi: 10.1029/92JB02280.

Calvès, G., Schwab, A.M., Huuse, M., Clift, P.D., Gaina, G., Jolley, D., Tabrez, A.R., & Inam, A. (2011). Seismic volcanostratigraphy of the western Indian rifted margin: The pre-Deccan igneous province. *Journal of Geophysical Research-Solid Earth*, 116, B01101. doi: 10.1029/2010JB000862.

Cartwright, J., Huuse, M., & Aplin, A. (2007). Seal bypass systems. *AAPG Bulletin*, 91, 1141-1166. doi: 10.1306/04090705181.

Deng, P., Mei, L.F., Liu, J., Zheng, J.Y., Liu, M.H., Cheng, Z.J., & Guo, F.T. (2018). Episodic normal faulting and magmatism during the syn-spreading stage of the Baiyun sag in Pearl River Mouth Basin: response to the multi-phase seafloor spreading of the South China Sea. *Marine Geophysical Research*, in press. doi, 10.1007/s11001-018-9352-9.

Franke, D. (2013). Rifting, lithosphere breakup and volcanism: comparison of magma-poor and volcanic rifted margins. *Marine and Petroleum Geology*, 43, 63-87. doi: 10.1016/j.marpetgeo.2012.11.003.

Hasenclever, J., Knorr, G., Rupke, L.H., Kohler, P., Morgan, J., Garofalo, K., Barker, S., Lohmann, G., & Hall, I.R.

(2017). Sea level fall during glaciation stabilized atmospheric CO_2 by enhanced volcanic degassing. *Nature Communications*, 8, 15867. doi: 10.1038/ncomms15867.

Holford, S.P., Schofield, N., MacDonald, J.D., Duddy, I.R., & Green, P.F. (2012). Seismic analysis of igneous systems in sedimentary basins and their impacts on hydrocarbon prospectivity: Examples from the southern Australian margin. *APPEA Journal*, 52, 229-252. doi: 0.1071/AJ11017.

Holford, S.P., Schofield, N., & Reynolds, P. (2017). Subsurface fluid flow focused by buried volcanoes in sedimentary basins: Evidence from 3D seismic data, Bass Basin, offshore southeastern Australia. *Interpretation*, 5, SK39-SK50. doi: 10.1190/INT-2016-0205.1.

Huang, B.J., Xiao, X.M., & Zhang, M.Q. (2003). Geochemistry, grouping and origins of crude oils in the Western Pearl River Mouth Basin, offshore South China Sea. *Organic Geochemistry*, 34, 993-1008. doi: 10.1016/S0146-6380(03)00035-4.

Isola, I., Mazzarini, F., Bonini, M., & Corti, G. (2014). Spatial variability of volcanic features in early-stage rift settings: the case of the Tanzania Divergence, East African rift system. *Terra Nova*, 26, 461-468. doi: 10.1111/ter.12121.

Iyer, K., Schmid, D.W., Planke,S., & Millett, J. (2017). Modelling hydrothermal venting in volcanic sedimentary basins: Impact on hydrocarbon maturation and paleoclimate. *Earth and Planetary Science Letters*, 467, 30-42. doi: 10.1016/j.epsl.2017.03.023.

Jackson C.A-L., Schofield, N., & Golenkov, B. (2013). Geometry and controls on the development of igneous sill-related forced folds: A 2-D seismic reflection case study from offshore southern Australia. *Geological Society of America Bulletin*, 125, 1874-1890. doi: 10.1130/B30833.1.

Jamtveit, B., Svensen, H., Podladchikov, Y.Y., & Planke, S. (2004). Hydrothermal vent complexes associated with sill intrusions in sedimentary basins. In: Breitkreuz, C., Petford, N. (Eds.), Physical Geology of High-Level

Magmatic Systems. Geological Society Publishing House, Bath, pp.233-241.

Judd, A.G., & Hovland, M. (2007). Seabed Fluid Flow: The Impact on Geology, Biology and the Marine Environment. Cambridge University Press, Cambridge, pp. 163-178.

Le Corvec, N., Spörli, K.B., Rowland, J., & Lindsay, J. (2013). Spatial distribution and alignments of volcanic centers: Clues to the formation of monogenetic volcanic fields. *Earth-Science Reviews*, 124, 96-114. doi: 10.1016/j.earscirev.2013.05.005.

Lester, R., Van Avendonk, H.J.A., McIntosh, K., Lavier, L., Liu, C.-S., Wang, T.K., & Wu, F. (2014). Rifting and magmatism in the northeastern South China Sea from wide-angle tomography and seismic reflection imaging. *Journal of Geophysical Research: Solid Earth*, 119, 2305-2323. doi: 10.1002/2013JB010639.

Li, C.F., Xu, X., Lin, J., Sun, Z., Zhu, J., Yao, Y.J., Zhao, X.X., Liu, Q.S., Kulhanek, D.K., Wang, J., Song, T.R., Zhao, J.F., Qiu, N., Guan, Y.X., Zhou, Z.Y., Williams, T., Bao, R., Briais, A., Brwon E.A., Chen, Y.F., Clift, P.D., Colwell, F.S., Dadd, K.A., Ding, W.W., Almeida, I.H., Huang, X.L., Hyun, S.M., Jiang, T., Koppers, A.A.P., Li, Q.Y., Liu, C.L., Liu, Z.F., Nagai, R.H., Peleo-Alampay, A., Su, X., Tejada, M.L.G., Rrinh, H.S., Yeh, Y.C., Zhang, C.L., Zhang, F., & Zhang, G.L. (2014). Ages and magnetic structures of the South China Sea constrained by the deep tow magnetic surveys and IODP Expedition 349. *Geochemistry, Geophysics, Geosystems*, 15, 4958-4983. doi: 10.1002/2014GC005567.

Lüdmann, T., & Wong, H.K. (1999). Neotectonic regime at the passive continental margin of northern South China Sea. *Tectonophysics*, 311, 113-138. doi: 10.1016/S0040-1951(99)00155-9.

Ma, B.J., Wu, S.G., Betzler, C., Qin, Z.L., Mi, L.J., Gao, W., Bai, H.Q., Wu, F., & Dong, D.D. (2018). Geometry, internal architecture, and evolution of buried volcanic mounds in the northern South China Sea. *Marine and Petroleum Geology*, 97, 540-555. doi: 10.1016/j.marpetgeo.2018.07.029.

Magee, C., Duffy, O.B., Purnell, K., Bell, R.E., Jackson, C.A.-L., & Reeve, M.T. (2016). Fault-controlled fluid flow inferred from hydrothermal vents imaged in 3D seismic reflection data, offshore NW Australia. *Basin Research*, 28, 299-318. doi: 10.1111/bre.12111.

Magee, C., Hunt-Stewart, E., & Jackson, C.A.-L. (2013a). Volcano growth mechanisms and the role of sub-volcanic intrusions: Insights from 2D seismic reflection data. *Earth and Planetary Science Letters*, 373, 41-53. doi: 10.1016/j.epsl.2013.04.041.

Magee, C., Jackson, C.A.-L., & Schofield, N. (2013b). The influence of normal fault geometry on igneous sill emplacement and morphology. *Geology*, 41, 407-410. doi: 10.1130/G33824.1.

Magee, C., Muirhead, D., Karvelas, A., Holford, S.P., Jackson, C.A.L., Bastow, I.D., Schofield, N., Stevenson, C.T.E., McLean, C., McCarthy, W., & Shtukert, O. (2016). Lateral magma flow in mafic sill complexes. *Geosphere*, 12, 809-841. doi: 10.1130/GES01256.1.

Millett, J.M., Wilkins, A.D., Campbell, E., Hole, M.J., Taylor, R.A., Healy, D., Jerram, D.A., Jolley, D.W., Planke, S., Archer, S.G., & Blischke, A. (2016). The geology of offshore drilling through basalt sequences: Understanding operational complications to improve efficiency: *Marine and Petroleum Geology*, 77, 1177-1192. doi: 10.1016/j.marpetgeo.2016.08.010.

Moussallam, Y., Tamburello, G., Peters, N., Apaza, F., Schipper, C.I., Curtis, A., Aiuppa, A., Masias, P., Boichu, M., Bauduin, S., Barnie, T., Bani, P., Giudice, G., & Moussallam, M. (2017). Volcanic gas emissions and degassing dynamics at Ubinas and Sabancaya volcanoes; implications for the volatile budget of the central volcanic zone. *Journal of Volcanology and Geothermal Research*, 343, 181-191. doi: 10.1016/j.jvolgeores.2017.06.027.

Pang, X., Chen, C., Peng, D., Zhu, M., Shu, Y., He, M., Shen, J., & Liu, B. (2007). Sequence stratigraphy of deep-water fan system of Pearl River, South China Sea. *Earth Science Frontier*, 14, 220-229 (in Chinese with English abstract).

Pang, X., Chen, C.M., Peng, D.J., Zhou, D., Shao, L., He, M., & Liu, B.J. (2008). Basic geology of Baiyun deep-water area in the northern South China Sea. *China Offshore Oil & Gas*, 20, 216-222 (in Chinese with English abstract).

Planke, S., Rasmussen, T., Rey, S.S., & Myklebust, R. (2005). Seismic characteristics and distribution of volcanic intrusions and hydrothermal vent complexes in the Vøing and Møre basins. In: Dorj A.G., Vining, B.A. (Eds.), Petroleum Geology: North-Western Europe and Global Perspectives? Proceedings of the 6th Petroleum Geology Conference. Geological Society, London.

Phillips, T.B., Magee, C., Jackson, C.A.L., & Bell, R.E. (2018). Determining the three-dimensional geometry of a dike swarm and its impact on later rift geometry using seismic reflection data. *Geology*, 46, 119-122. doi: 10.1130/G39672.1.

Qin, G.Q. (1996). Application of micropaleontology to the sequence stratigraphic studies of late Cenozoic in the Zhujiang River Mouth Basin. *Marine Geology & Quaternary Geology*, 16, 1-17 (in Chinese with English Abstract).

Qin, G.Q. (2000). Comments on "Discussion on the Upper-Lower Tertiary boundary in Well BY7-1" of the Pearl River Mouth Basin. Journal of Stratigraphy, 24, 387-393 (in Chinese with English Abstract).

Rateau, R., Schofield, N., & Smith, M. (2013). The potential role of igneous intrusions on hydrocarbon migration, West of Shetland. *Petroleum Geosciences*, 19, 259-272. doi: 10.1144/petgeo2012-035.

Reynolds, P., Schofield, N., Brown, R.J., & Holford, S.P. (2018). The architecture of submarine monogenetic volcanoes - insights from 3D seismic data. *Basin Research*, 30, 437-451. doi: 10.1111/bre.12230.

Schofield, N., Holford, S., Millett, J., Brown, D., Jolley, D., Passey, S., Muirhead, D., Grove, C., Magee, C., Murray, J., Hole, M., Jackson, C., & Stevenson, C. (2017). Regional magma plumbing and emplacement mechanisms of the Faroe-Shetland Sill Complex: Implications for magma transport and petroleum systems within sedimentary basins. *Basin Research*, 29, 41-63. doi: 10.1111/bre.12164.

Sibuet, J.C., Yeh, Y.C., & Lee, C.S. (2016). Geodynamics of the South China Sea. *Tectonophysics*, 692, 98-119. doi: 10.1016/j.tecto.2016.02.022.

Sibuet, J.C., Hsu, S.K., Le Pichon, X., Le Formal, J.P., Reed, D., Moore, G., & Liu, C.S. (2002). East Asia plate tectonics since 15 Ma: constraints from the Taiwan region. *Tectonophysics*, 344, 103-134. doi: 10.1016/S0040-1951(01)00202-5.

Sun, Z., Xu, Z., Sun, L., Pang, X., Yan, C., Li, Y., Zhao, Z., Wang, Z., & Zhang, C. (2014a). The mechanism of post-rift fault activities in Baiyun Sag, Pearl River Mouth Basin. *Journal of Asian Earth Sciences*, 89, 76-87. doi: 10.1016/j.jseaes.2014.02.018.

Sun, Q.L., Wu, S.G., Cartwright, J., & Dong, D.D. (2012). Shallow gas and focused fluid flow systems in the Pearl River Mouth basin, northern South China Sea. *Marine Geology*, 315, 1-14. doi : 10.1016/j.margeo.2012.05.003.

Sun, Q.L., Wu, S.G., Cartwright, J., Wang, S.H., Lu, Y.T., Chen, D.X., & Dong, D.D. (2014b). Neogene igneous intrusions in the northern South China Sea: evidence from high resolution three dimensional seismic data. *Marine and Petroleum Geology*, 54, 83-95. doi: 10.1016/j.marpetgeo.2014.02.014.

Svensen, H., Planke, S., Jamtveit, B., & Pedersen, T. (2003). Seep carbonate formation controlled by hydrothermal vent complexes: A case study from the Vøing Basin, the Norwegian Sea. *Geo-Marine Letters*, 23, 351-358. doi: 10.1007/s00367-003-0141-2.

Svensen, H., Planke, S., Malthe-Sorenssen, A., Jamtveit, B., Myklebust, R., Rasmussen Eidem, T., & Rey, S.S. (2004). Release of methane from a volcanic basin as a mechanism for initial Eocene global warming. *Nature*, 429, 542-545. doi:

Svensen, H., Corfu, F., Polteau, S., Hammer, O., & Planke, S. (2012). Rapid magma emplacement in the Karoo Large Igneous Province. *Earth Planetary Science Letters*, 325, 1-9. doi: 10.1038/nature02566.

Tissot, B.P., & Welte, D.H. (1984). Petroleum Formation and Occurrence. Springer, Berlin, pp. 74-266.

White, N., Thompson, M., & Barwise, T. (2003). Understanding the thermal evolution of deep-water continental margins. *Nature*, 426, 334-343. doi: 10.1038/nature02133.

Yan, P., Deng, H., Liu, H., Zhang, Z., & Jiang, Y. (2006). The temporal and spatial distribution of volcanism in the South China Sea region. *Journal of Asian Earth Science*, 27, 647-659. doi: 10.1016/j.jseaes.2005.06.005.

Yang, J.F., Zhu, W.B., Guan, D., Zhu, B.B., Yuan, L.S., Xiang, X.M., Su, J.B., He, J.W., & Wu, X.H. (2016). 3D seismic interpretation of subsurface eruptive centers in a Permian large igneous province, Tazhong Uplift, central Tarim Basin, NW China. *International Journal of Earth Sciences*, 105, 2311-2326. doi: 10.1007/s00531-015-1289-5.

Yu, H.S. (1994). Structure, stratigraphy and basin subsidence of Tertiary basins along the Chinese southeastern continental margin. *Tectonophysics*, 253, 63-76. doi: 10.1016/0040-1951(94)90017-5.

Zhang, Q.X., & Huang, B.J. (1991). Genetic types and generation history of natural gases from major basins in the South China Sea. *China Offshore Oil & Gas*, 4, 5-13 (in Chinese with English Abstract).

Zhao, F., Alves, T.M., Wu, S.G., Li, W., Huuse, M., Mi, L.J., Sun, Q.L., & Ma, B.J. (2016). Prolonged post-rift magmatism on highly extended crust of divergent continental margins (Baiyun Sag, South China Sea). *Earth and Planetary Science Letters*, 445, 79-91. doi: 10.1016/j.epsl.2016.04.001.

Zhao, F., Wu, S.G., Sun, Q.L., Huuse, M., Li, W., & Wang, Z.J. (2014). Submarine volcanic mounds in the Pearl River Mouth Basin, northern South China Sea. *Marine Geology*, 355, 162-172. doi: 10.1016/j.margeo.2014.05.018.

Zhao, M., He, E., Sibuet, J.-C., Sun, L., Qiu, X., Tan, P., & Wang, J. (2018). Postseafloor spreading volcanism in the central east South China Sea and its formation through an extremely thin oceanic crust. *Geochemistry, Geophysics, Geosystems*, 19, 621-641. doi: 10.1002/2017GC007034.

Zhao, S.J., Wu, S.G., Shi, H.S., Dong, D.D., & Chen, D.X. (2012). Structures and dynamic mechanism related to the dongsha movement at the northern margin of South China Sea. *Progress in Geophysics*, 27, 1008-1019 (in Chinese with English abstract).

Zhu, W., Huang, B., Mi, L., Wilkins, R.W.T., Fu, N., & Xiao, X. (2009). Geochemistry, origin, and deep-water exploration potential of natural gases in the Pearl River Mouth and Qiongdongnan Basins, South China Sea. *AAPG Bulletin*, 93, 741-761. doi: 10.1306/02170908099.

Zou, H., Li, P., & Rao, C. (1995). Geochemistry of Cenozoic volcanic rocks in Zhu Jiangkou basin and its geodynamic significance. *Geochimica*, 24, 33-45.

Figure Captions

Figure 1: (a) Geological setting and subdivision of the Pearl River Mouth Basin (enlargement of pink square in the top left corner). The study area (red square: 3D seismic survey) is located in the Yunkai Low Massif between the Kaiping Sag and the Baiyun Sag. The boundary faults are modified from Pang et al. (2007) and Sun et al. (2014a). Top left: Geological backgrounds of the South China Sea. (b) Schematic stratigraphic column of the Pear River Mouth Basin (modified from Pang et al. (2008) and Sun et al. (2014b)). SR = seismic reflectors, TE= tectonic evolution, BE = basin evolution, DE= sedimentary environment. (c) Geoseismic interpretation of the study area; see (a) for location.

Figure 2: Correlation of seismic profile and borehole (BY7-1). Five layers of free gases (mainly shown as enhanced negative seismic anomalies or blanking reflection with low frequency) are drilled by BY7-1, which can also be identified in the well loggings and geochemical analysis. The items marked with ® and © (Lithology, K-Ar dating, Ages and depositional environments (DEs), $\delta^{13}C$ (planktonic foraminifera) and $\delta^{18}O$ (planktonic foraminifera)) are modified from Qin. (1996) and Qin. (2000). Parts of the well loggings are also used in Qin. (1996), Qin. (2000) and Zhao et al. (2016). The item ($\delta^{13}C$) marked with§ is from the analysis of headspace gas.

Figure 3: Three-dimensional visualization of the top of volcano complexes (Surface T5). The volcano complexes show as positive reliefs. Normal faults which present as linear structures with sharp boundaries are also observed.

Figure 4: (a)-(d): Seismic characteristics of free gas, normal faults and volcano complexes. See locations of (a)-(c) in Fig. 5i and location of (d) in Fig. 5a. Free gas shows as stacked or isolated enhanced seismic anomalies with low frequencies. It distributes in several layers and its extent is outlined by normal faults. Sometimes, wipe-out zone (blanking seismic reflections) and pull-down seismic reflections are observed underneath the enhanced seismic anomalies. Faults are denser within the strata above volcano complexes (light green polygon). Some large normal faults can penetrate into the basement and they extend upward to surface T0. The semi-transparent green and blue squares are the windows of RMS amplitudes of Fig. 5g and Fig. 5h, respectively. Variance slice locations of Fig. 5c (straight dashed blue line) and Fig. 5d (straight dashed red line) are also labeled.

Figure 5: The configurations of volcano complexes, free gas and normal faults. (a) Top of volcano complexes (Surface T5). The volcano complexes show as positive reliefs; (b) Thickness of the volcano complexes, which shows that the volcano complexes linearly trend NW-SE; (c) and (d) variance slices of 1150 ms and 1800 ms (in the post-eruption strata). Faults can be clearly observed; (e) variance slice of 30 ms below the base of volcano complexes (in the pre-eruption strata) and faults are also clearly identified; (f) RMS amplitude (1150 ms with windows of ±25 ms) of the entire 3D survey. The free gas has very high RMS amplitude and it only distributes in the southeastern part of the 3D seismic survey; (g) and (h): RMS amplitude of 1150 ms with windows of ±50 ms and 1800 ms with windows of ±100 ms. Free gas shows as high values of RMS amplitude (warm colors). See locations in Fig. (a); (g) and (h): outlines of volcano complexes and

interpreted faults are superimposed on the RMS amplitude maps. Free gas is usually limited by faults and locates within the extents of volcano complexes.

Figure 6: (a) and (b) uninterpreted and interpreted profiles show seismic characteristics of the strata above the volcano complex. See location in Fig. 5a. These strata are bended and normal faults densely occurred within these strata. Free gas is closely linked to the normal faults and the seismic reflections below free gas are blanking or wipe-out. The semi-transparent green and blue squares are the windows of RMS amplitudes of Fig. 5g and Fig. 5h, respectively. Variance slice locations of Fig. 5c (straight dashed blue line) and Fig. 5d (straight dashed red line) are also labeled.

Figure 7: (a) Normal faults crosscut the volcano complex and (b) Its line drawing. The eruptive materials in the hanging wall are thicker than its footwall counterpart. See location in Fig. 5i; (c) Normal faults immediately terminated at the base of volcano complexes and (d) Its line drawing. See location in Fig. 5a.

Figure 8: (a)-(c): Fault strikes of Figure 5e (n = 202), 5c (n = 90) and 5d (n = 196). Both the faults within the pre-eruption and post-eruption strata have similar strikes (NWW-SEE); (d)-(f): Fault lengths of Figure 5e, 5c and 5d. The faults have small scales and usually below 3 km long; (h)-(j): Fault strike vs fault length of Figure 5e, 5c and 5d.

Figure 9: Model for the magmation, faulting and focused fluid flow in the study area. (a) Fault fed

pioneer magma extruded in the shallow water at a very early stage; (b) In the quiescent stage, detrital sediments deposited on the pioneer eruptive materials; (c) Large-scale magma extruded onto the paleo-seabed and formed the mounded volcano complexes; (d) Thermogenic hydrocarbon accumulated to the volcano complexes or the traps above it. Faulting directly occurred within the strata above volcano complex and hydrocarbon leakage through these faults. Please see details in the text.

Figure 1

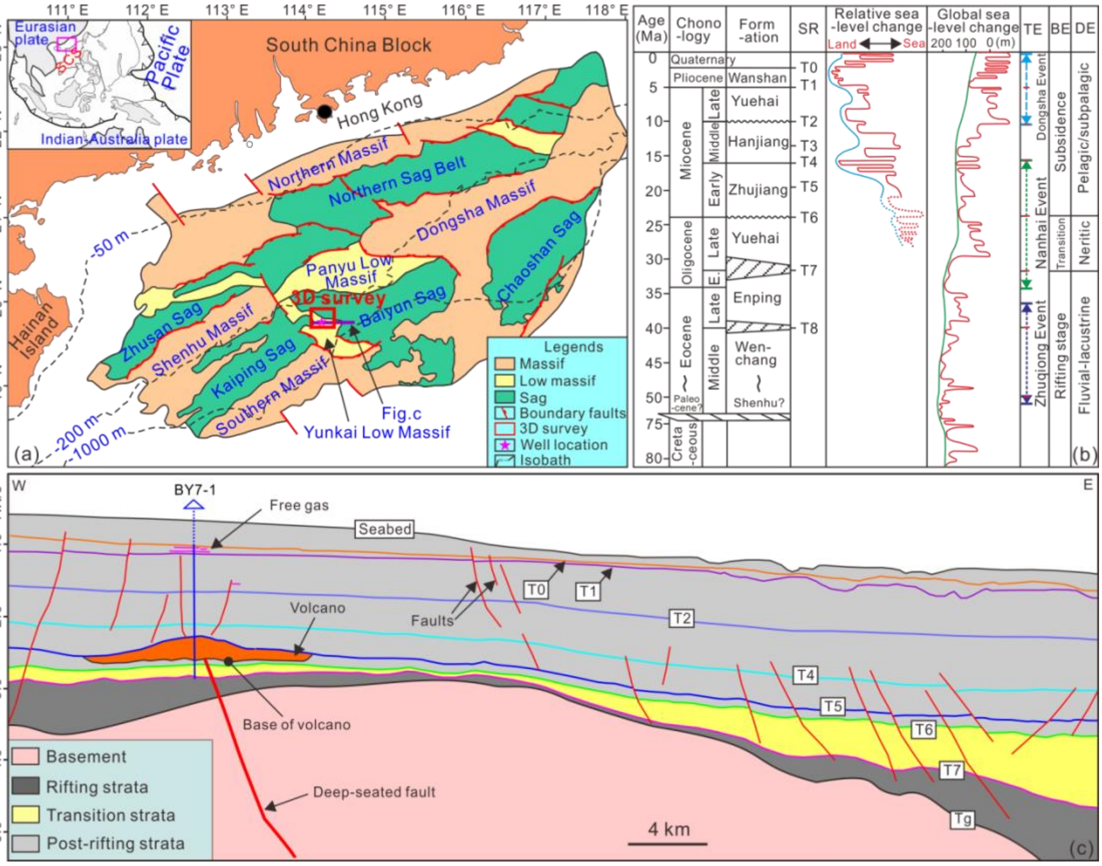

Figure 1: (a) Geological setting and subdivision of the Pearl River Mouth Basin (enlargement of pink square in the top left corner). The study area (red square: 3D seismic survey) is located in the Yunkai Low Massif between the Kaiping Sag and the Baiyun Sag. The boundary faults are modified from Pang et al. (2007) and Sun et al. (2014a). Top left: Geological backgrounds of the South China Sea. (b) Schematic stratigraphic column of the Pear River Mouth Basin (modified from Pang et al. (2008) and Sun et al. (2014b)). SR = seismic reflectors, TE= tectonic evolution, BE = basin evolution , DE= sedimentary environment. (c) Geoseismic interpretation of the study area; see (a) for location. Uninterpreted version provided in the Supplementary Fig. S1.

Figure 2

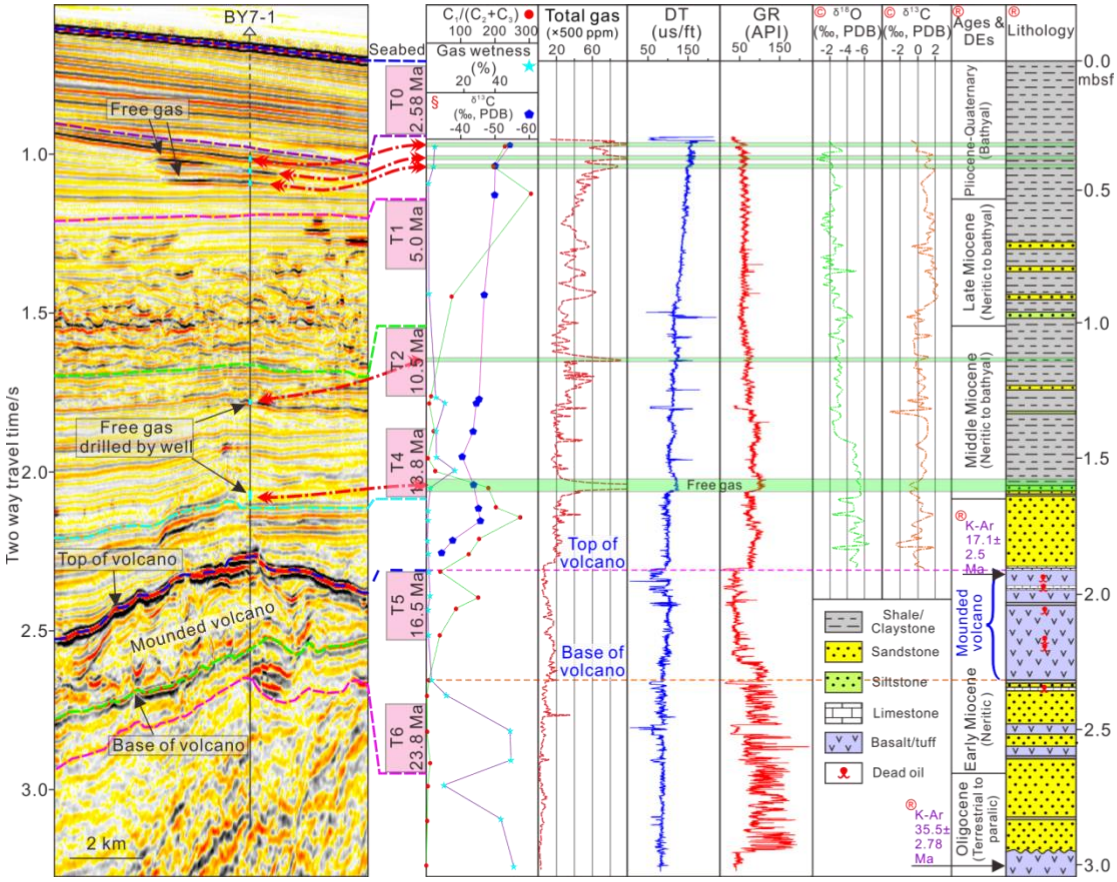

Figure 2: Correlation of seismic profile and borehole (BY7-1). Five layers of free gases (mainly shown as enhanced negative seismic anomalies or blanking reflection with low frequency) are drilled by BY7-1, which can also be identified in the well loggings and geochemical analysis. The items marked with ® and © (Lithology, K-Ar dating, Ages and depositional environments (DEs), $\delta^{13}C$ (planktonic foraminifera) and $\delta^{18}O$ (planktonic foraminifera)) are modified from Qin. (1996) and Qin. (2000). Parts of the well loggings are also used in Qin. (1996), Qin. (2000) and Zhao et al. (2016). The item ($\delta^{13}C$) marked with§ is from the analysis of headspace gas.

Figure 3

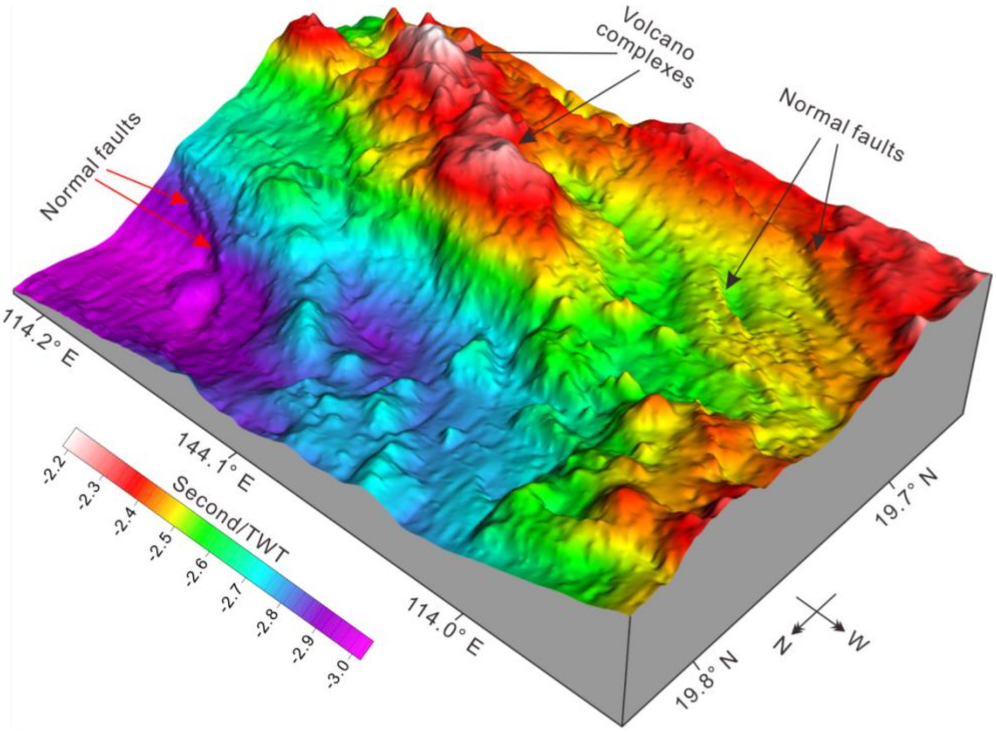

Figure 3: Three-dimensional visualization of the top of volcano complexes (Surface T5). The volcano complexes show as positive reliefs. Normal faults which present as linear structures with sharp boundaries are also observed.

Figure 4

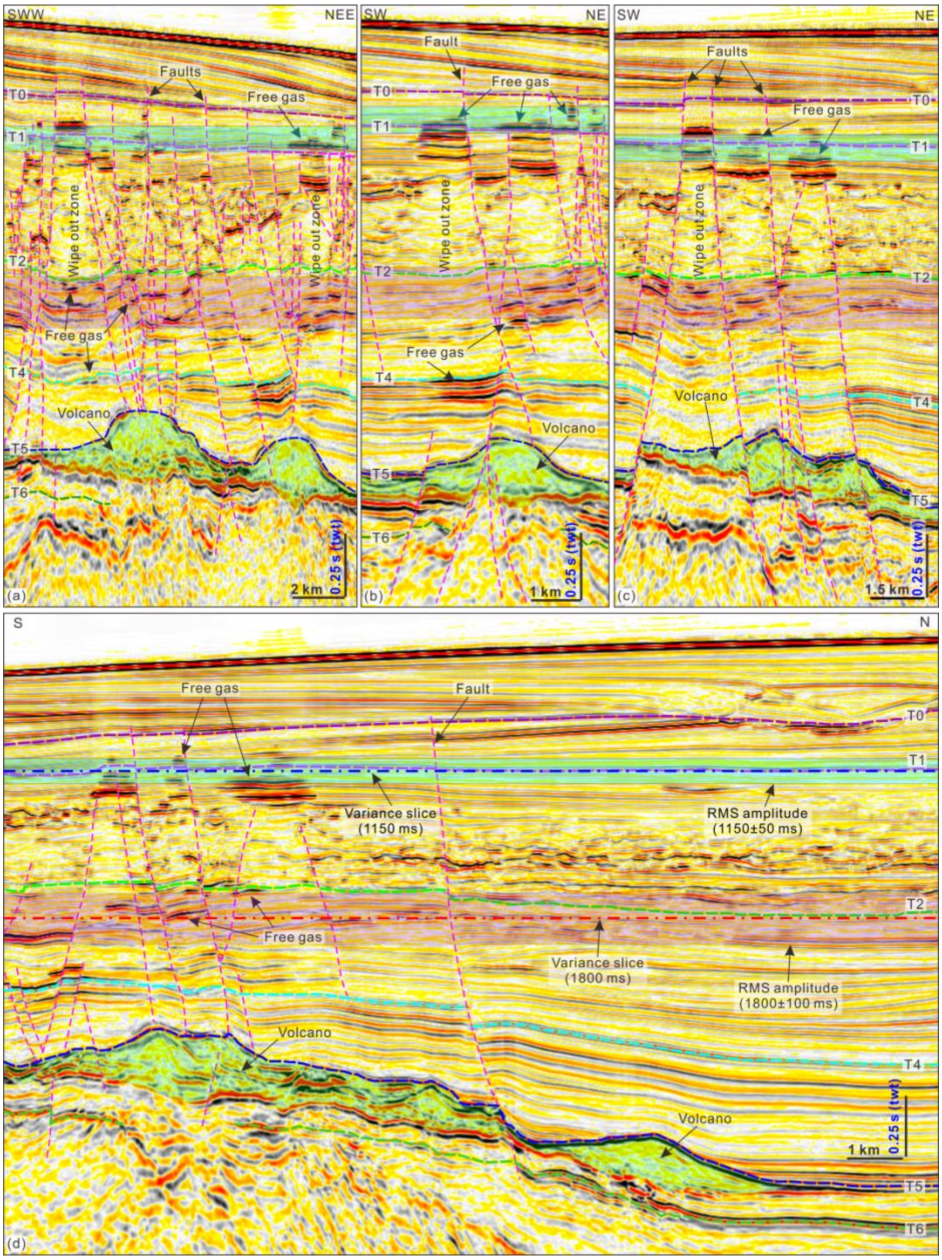

Figure 4: (a)-(d): Seismic characteristics of free gas, normal faults and volcano complexes. See locations of (a)-(c) in Fig. 5i and location of (d) in Fig. 5a. Free gas shows as stacked or isolated enhanced seismic anomalies with low frequencies. It distributes in several layers and its extent is outlined by normal faults. Sometimes, wipe-out zone (blanking seismic reflections) and pull-down seismic reflections are observed underneath the enhanced seismic anomalies. Faults are denser within the strata above volcano complexes (light green polygon). Some large normal faults can penetrate into the basement and they extend upward to surface T0. The semi-transparent green and blue squares are the windows of RMS amplitudes of Fig. 5g and Fig. 5h, respectively. Variance slice locations of Fig. 5c (straight dashed blue line) and Fig. 5d (straight dashed red line) are also labeled.

Figure 5

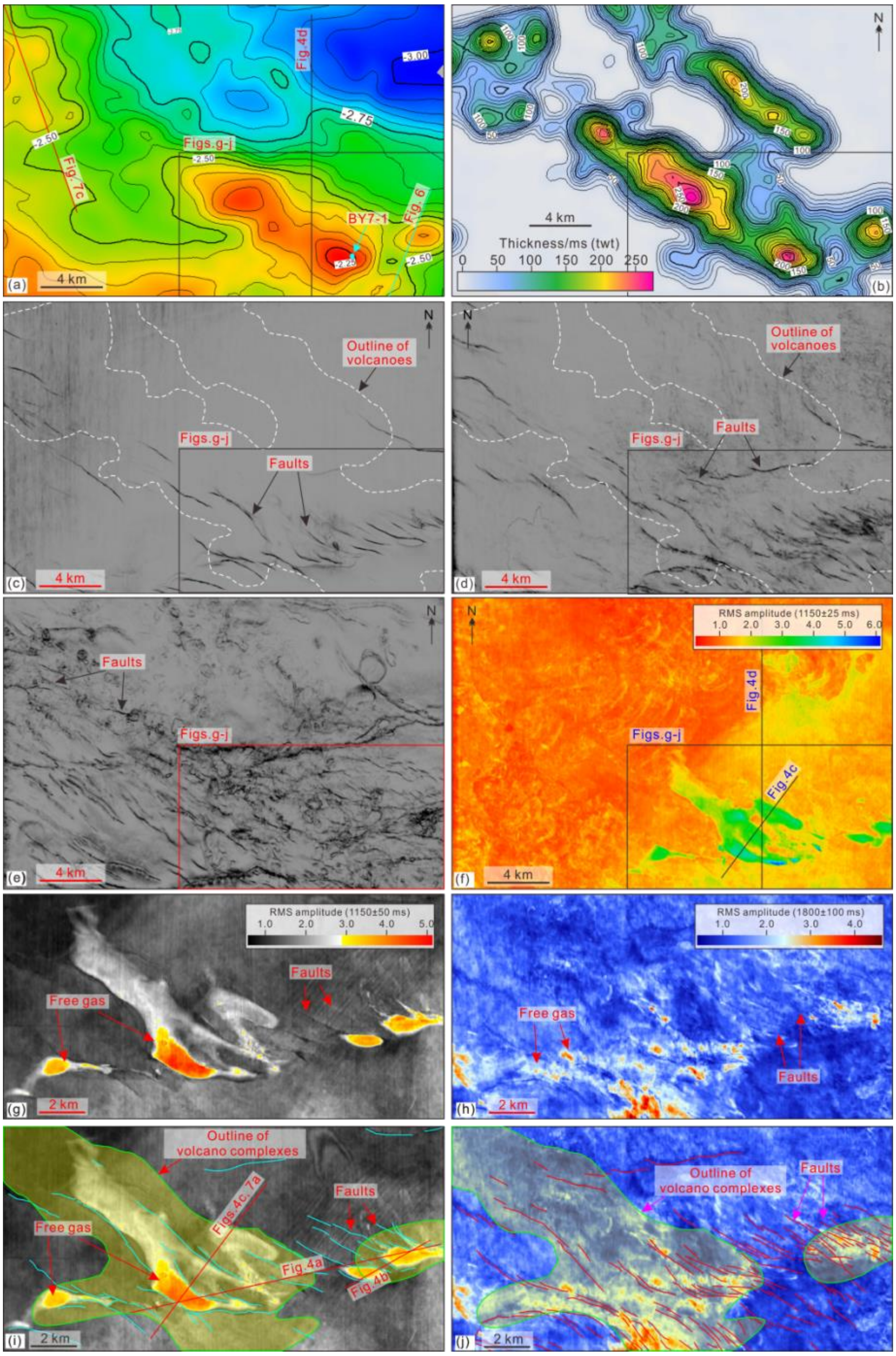

Figure 5: The configurations of volcano complexes, free gas and normal faults. (a) Top of volcano complexes (Surface T5). The volcano complexes show as positive reliefs; (b) Thickness of the volcano complexes, which shows that the volcano complexes linearly trend NW-SE; (c) and (d) variance slices of 1150 ms and 1800 ms (in the post-eruption strata). Faults can be clearly observed; (e) variance slice of 30 ms below the base of volcano complexes (in the pre-eruption strata) and faults are also clearly identified; (f) RMS amplitude (1150 ms with windows of ±25 ms) of the entire 3D survey. The free gas has very high RMS amplitude and it only distributes in the southeastern part of the 3D seismic survey; (g) and (h): RMS amplitude of 1150 ms with windows

of ±50 ms and 1800 ms with windows of ±100 ms. Free gas shows as high values of RMS amplitude (warm colors). See locations in Fig. (a); (g) and (h): outlines of volcano complexes and interpreted faults are superimposed on the RMS amplitude maps. Free gas is usually limited by faults and locates within the extents of volcano complexes.

Figure 6

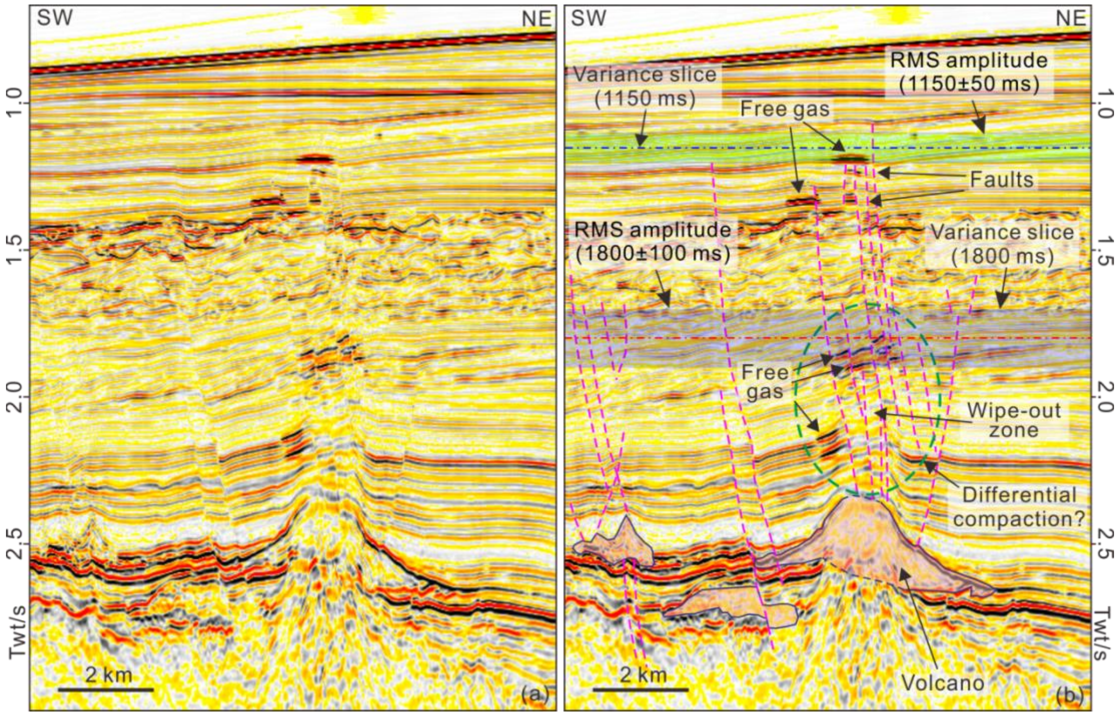

Figure 6: (a) and (b) uninterpreted and interpreted profiles show seismic characteristics of the strata above the volcano complex. See location in Fig. 5a. These strata are bended and normal faults densely occurred within these strata. Free gas is closely linked to the normal faults and the seismic reflections below free gas are blanking or wipe-out. The semi-transparent green and blue squares are the windows of RMS amplitudes of Fig. 5g and Fig. 5h, respectively. Variance slice locations of Fig. 5c (straight dashed blue line) and Fig. 5d (straight dashed red line) are also labeled.

Figure 7

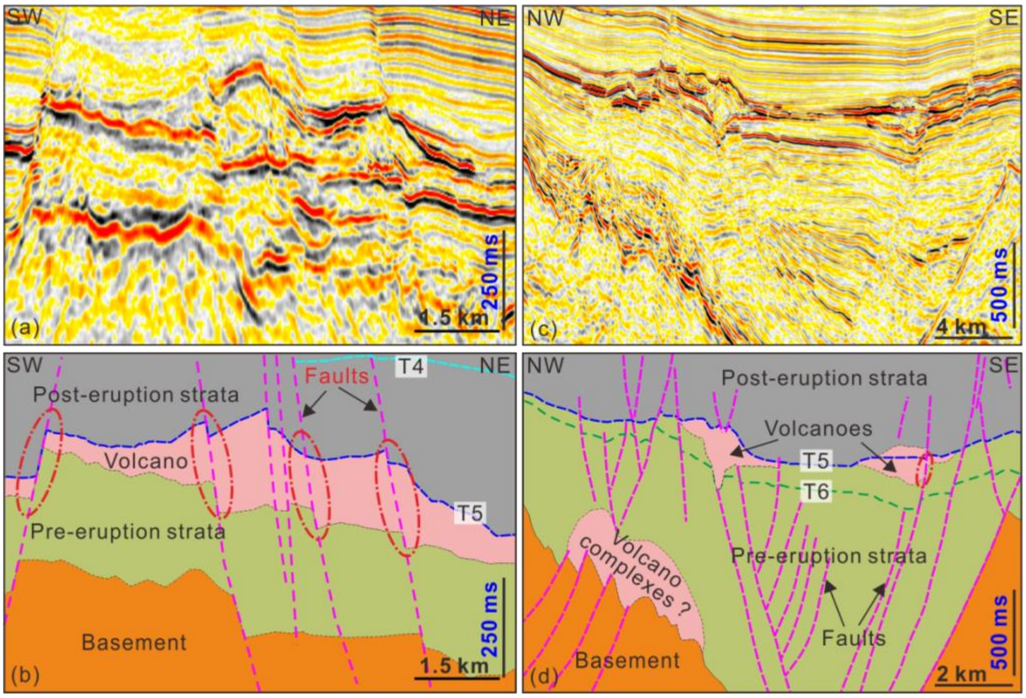

Figure 7: (a) Normal faults crosscut the volcano complex and (b) Its line drawing. The eruptive materials in the hanging wall are thicker than its footwall counterpart; (c) Normal faults immediately terminated at the base of volcano complexes and (d) Its line drawing.

Figure 8

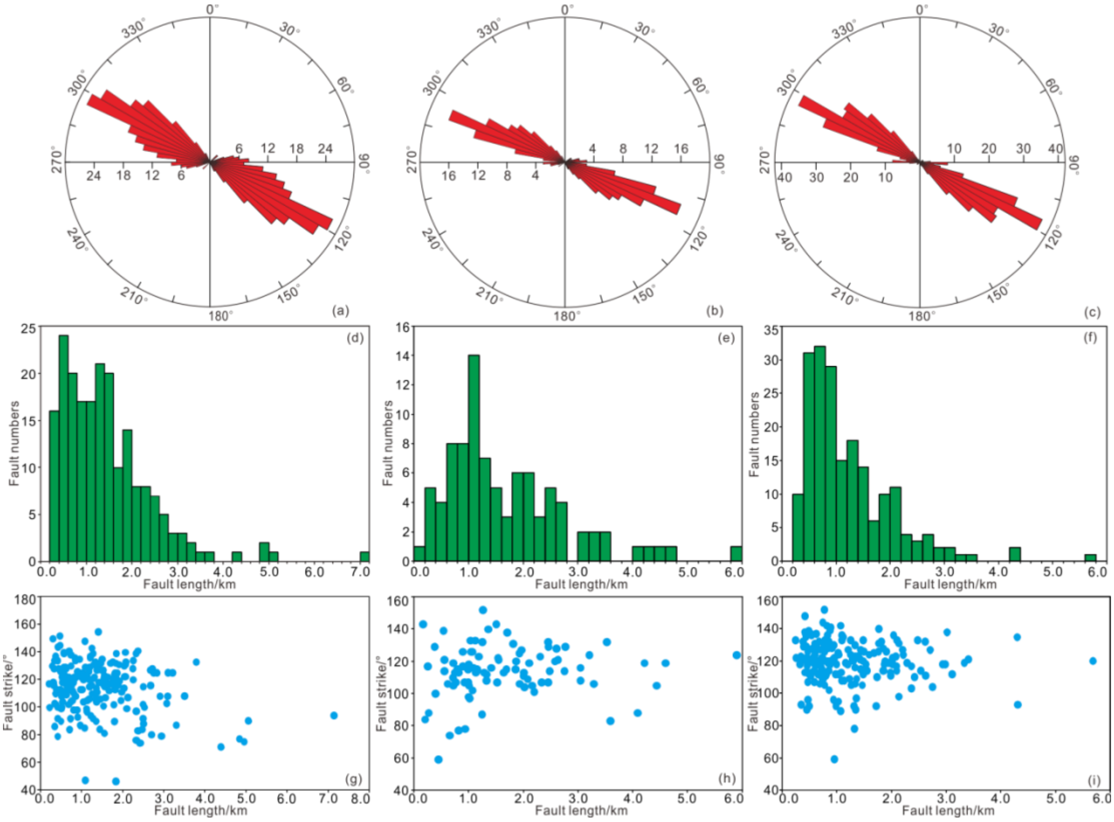

Figure 8: (a)-(c): Fault strikes of Figure 5e (n = 202), 5c (n = 90) and 5d (n = 196). Both the faults within the pre-eruption and post-eruption strata have similar strikes (NWW-SEE); (d)-(f): Fault lengths of Figure 5e, 5c and 5d. The faults have small scales and usually blow 3 km long; (h)-(j): Fault strike vs fault length of Figure 5e, 5c and 5d.

Figure 9

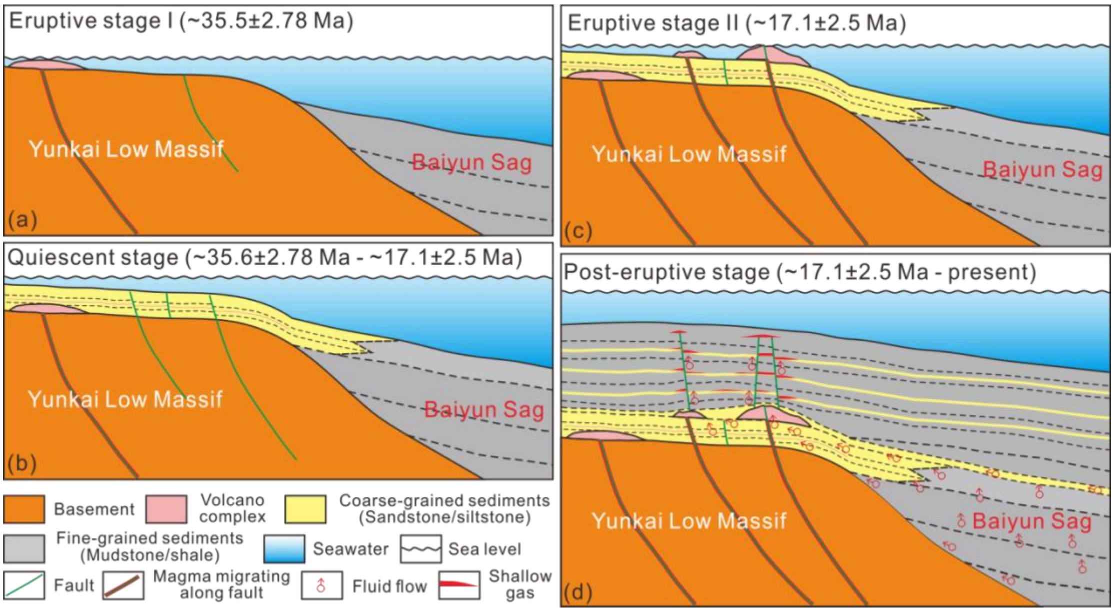

Figure 9: Model for the magmation, faulting and focused fluid flow in the study area. (a) Fault fed pioneer magma extruded in the shallow water at a very early stage; (b) In the quiescent stage, detrital sediments deposited on the pioneer eruptive materials; (c) Large-scale magma extruded onto the paleo-seabed and formed the mounded volcano complexes; (d) Thermogenic hydrocarbon accumulated to the volcano complexe or the traps above it. Faulting directly occurred within the strata above volcano complex and hydrocarbon leakage through these faults. Please see details in the text.